

# Journal of Materials Chemistry A

Accepted Manuscript



This is an *Accepted Manuscript*, which has been through the Royal Society of Chemistry peer review process and has been accepted for publication.

*Accepted Manuscripts* are published online shortly after acceptance, before technical editing, formatting and proof reading. Using this free service, authors can make their results available to the community, in citable form, before we publish the edited article. We will replace this *Accepted Manuscript* with the edited and formatted *Advance Article* as soon as it is available.

You can find more information about *Accepted Manuscripts* in the [Information for Authors](#).

Please note that technical editing may introduce minor changes to the text and/or graphics, which may alter content. The journal's standard [Terms & Conditions](#) and the [Ethical guidelines](#) still apply. In no event shall the Royal Society of Chemistry be held responsible for any errors or omissions in this *Accepted Manuscript* or any consequences arising from the use of any information it contains.

## Further Findings of X-ray Absorption Near-Edge Structure in Lithium Manganese Spinel Oxide using First-Principles Calculations †

Cite this: DOI: 10.1039/x0xx00000x

Received 00th January 2012,  
Accepted 00th January 2012

DOI: 10.1039/x0xx00000x

www.rsc.org/

Toyoki Okumura,\* Yoichi Yamaguchi, Masahiro Shikano, Hironori Kobayashi\*

X-ray absorption near-edge structure (XANES) spectroscopy, which reveals the features of the electronic and local structure, of lithium manganese oxides  $\text{Li}_x\text{Mn}_2\text{O}_4$  ( $x = 0 - 2$ ) was examined using first-principles calculations. Both the easily observable parts and the tiny peaks of the theoretical Mn  $K$ -edge XANES spectra agreed with the experimental spectra. From the theoretical results of two anti-ferromagnetic  $\text{LiMn}_2\text{O}_4$  models, the contributions of the  $\text{Mn}^{3+}$  ion and  $\text{Mn}^{4+}$  ion centers to the XANES spectra differ due to the difference in the overlap between the Mn  $4p$  partial density of state (PDOS) and the O  $2p$  PDOS. Similar results can be also seen by comparing the theoretical XANES spectra and the PDOS between  $\text{Li}(\text{Mn}^{3+}\text{Mn}^{4+})\text{O}_4$  and de-intercalated  $\text{Li}_{0.5}(\text{Mn}^{3+}_{0.5}\text{Mn}^{4+}_{1.5})\text{O}_4$  and  $\text{Mn}^{4+}_2\text{O}_4$  ( $\lambda$ - $\text{MnO}_2$ ). The XANES spectral changes with the lithium ion displacement (six- to four-coordination) due to the phase transition (cubic  $Fd-3m$   $\text{LiMn}_2\text{O}_4$  to tetragonal  $I4_1/amd$   $\text{Li}_2\text{Mn}_2\text{O}_4$ ) can be determined by the indirect contribution of the Li  $2p$  PDOS to the Mn  $4p$  PDOS via the O  $2p$  PDOS.

### 1. Introduction

X-ray absorption spectroscopy (XAS) analyzes the local structure around an absorbed atom and is therefore a powerful technique for investigating the electrochemical behavior in the materials of energy devices such as the lithium-ion battery (LIB). The XAS applications to such materials could be expanded because the use of synchrotron radiation provides detailed understanding of the electrochemical behavior over a short time scale (ms order)<sup>1-3</sup> and/or from small area ( $\mu\text{m}$  order)<sup>4,5</sup> possible. The spectrum measured by XAS is separated into the X-ray absorption near-edge structure (XANES) and extended X-ray absorption fine structure (EXAFS) spectroscopies based on the energy distance from an absorption edge. The local atomic environment around the absorbed-center redox ion has been commonly determined by EXAFS, while XANES has been used for identifying the valence state.<sup>6</sup> Actually, the XANES also involves the atomic environmental contributions such as the ligand-type, geometry, coordination number, bonding length, and bond covalence. These additional findings of the XANES spectrum are useful in discussing electrochemical structural changes when the spectrum is measured at short time scale and/or from small area because the weak EXAFS oscillation is difficult to analyze even when brilliant synchrotron radiation is used. This idea would be especially important for discussing the spectrum combined with electrochemical *in-situ* measurements.

Computational simulations can be an effective method for the visualizing the XANES spectra that reflect the aforementioned local atomic environments.<sup>7</sup> Two different approaches for theoretically

estimating XANES spectra have been proposed: density functional theory (DFT) using supercells with or without the core hole, and multiple scattering theory. In our previous study, we adapt the DFT calculations to discuss the XANES spectra of two-type lithium cobalt oxides in which the number of stacked  $\text{CoO}_2$  layers differed, *i.e.*, three layers in  $\text{O3-LiCoO}_2$  and two layers in  $\text{O2-LiCoO}_2$ .<sup>8</sup> The differences in the shape of the XANES spectra along with differences in the structural symmetries and/or lithium contents were analyzed using DFT calculations. In particular, the symmetries studied were either  $\text{O3-}$  or  $\text{O2-}$  type, and the lithium content changed during the phase transition from  $\text{O2-LiCoO}_2$  to  $\text{T}^\#2\text{-Li}_{0.5}\text{CoO}_2$ . The resulting changes to the phase spectra could be determined by the overlap of the partial density of states (PDOS) between the Co  $4p$  orbital and the other orbitals.

The current application scope of LIBs has been expanded from consumer devices such as laptops and phones to transportation applications such as electric vehicles (EVs).<sup>9</sup> The spinel oxide  $\text{LiMn}_2\text{O}_4$  is one of the key positive electrodes in EV LIB applications:  $\text{LiMn}_2\text{O}_4$  achieves an excellent cycle performance by blending with  $\text{LiMO}_2$  ( $M = \text{Mn, Co, Ni etc.}$ )<sup>10-12</sup>, which has been recently embedded in commercialized EV. An understanding of the electrochemical behavior of  $\text{LiMn}_2\text{O}_4$  could be also extended to the analysis of related high-voltage electrodes such as  $\text{LiNi}_{0.5}\text{Mn}_{1.5}\text{O}_4$ .<sup>13,14</sup> Thereby, improving versatile structural analysis techniques, such as the XANES technique in the spinel oxide  $\text{LiMn}_2\text{O}_4$  origin, is vital for surveying the electrochemical behavior of these electrodes during battery performance tests.

The stoichiometric  $\text{LiMn}_2\text{O}_4$  spinel structure possesses the crystallographic space group  $Fd-3m$ . Manganese ions occupy  $16d$  octahedral sites and lithium ions occupy  $8a$  tetrahedral sites in a cubic close-packed array of oxygen ions. The manganese ions have two types of electron configurations around  $E_F$ , of which half are high spin  $3d^4 (t_{2g}^3 e_g^1)$  at  $\text{Mn}^{3+}$  ion and half are  $3d^3 (t_{2g}^3 e_g^0)$  at  $\text{Mn}^{4+}$  ion. Further, this was a small polaron semiconductor, where electronic conduction occurs *via* the hopping of electrons between the  $e_g$  orbitals on adjacent  $\text{Mn}^{3+}/\text{Mn}^{4+}$  ions.<sup>15,16</sup> Therefore, the average valence state of manganese ion in  $\text{LiMn}_2\text{O}_4$  is +3.5. Ohzuku *et al.* precisely examined the phase transformation of the electrochemical lithium-ion de-intercalation ( $0 < x \leq 1$ ) and intercalation processes ( $1 \leq x < 2$ ) from  $\text{Li}_x\text{Mn}_2\text{O}_4$  ( $x = 1$ ) based on *ex-situ* XRD measurements.<sup>17</sup> The de-intercalation slope could be separated into two regions (I and II). In region II, they observed continuous shrinking of the lattice volume of the  $Fd-3m$  phase,  $\text{Li}_x\text{Mn}_2\text{O}_4$  ( $\alpha \leq x \leq 1$ ), with the lithium-ion removal, which indicates a single-phase solid-solution reaction. Over  $x \leq \alpha$  (region I), a two-phase reaction caused the appearance of the other  $Fd-3m$  phase,  $\lambda\text{-MnO}_2$ . At the intercalation slope where  $1 \leq x < 2$  (region III), the reversible capacity limitation was caused by a phase transformation from the cubic  $Fd-3m$   $\text{LiMn}_2\text{O}_4$  phase to the tetragonal  $\text{Li}_2\text{Mn}_2\text{O}_4$  phase *via* a two-phase reaction. The phase transitions during de-intercalation and intercalation from  $\text{LiMn}_2\text{O}_4$  are summarized in ESI, Fig. S1.†

In the present study, we concentrate on the Mn  $K$ -edge XANES spectra of the electrochemical lithium-ion (de-)intercalated  $\text{Li}_x\text{Mn}_2\text{O}_4$ . We estimate the theoretical XANES spectra of several spinel oxide  $\text{Li}_x\text{Mn}_2\text{O}_4$  models using DFT calculations and discuss what local structures in the manganese-based electrode materials can be detected from the XANES spectra.

## 2. Experimental procedure

$\text{LiMn}_2\text{O}_4$  was synthesized *via* solid-state reactions.<sup>6</sup>  $\text{Li}_2\text{CO}_3$  (99.99% Kojundo Chemical Lab Industries) and  $\text{Mn}_2\text{O}_3$ , which was obtained by preheating  $\text{MnCO}_3$  (99.99% Kojundo Chemical Lab Industries) at  $600^\circ\text{C}$  for 48 h, were used as starting materials. The required amounts of the starting materials were mixed and heated at  $800^\circ\text{C}$  for 2 days in air and then cooled with a rate of  $0.5^\circ\text{C}/\text{min}$ . Synchrotron XAFS analyses of the pristine and electrochemically reacted lithium manganese spinel oxide samples were then carried out to investigate the lithium-ion (de-)intercalation processes. The electrode was composed by a suspension containing 80 wt% active material, 10 wt% acetylene black, and 10 wt% polyvinylidene difluoride, which was coated and then pressed on an aluminum foil. The electrodes were assembled in a two-electrode cell using metallic lithium foil as a counter/reference electrode. The liquid electrode was  $1 \text{ mol dm}^{-3}$  ethylene carbonate/dimethyl carbonate solution of  $\text{LiPF}_6$ . Electrochemical (de-)intercalation of the lithium ion was carried out at a constant current rate of 0.1 C (about  $0.067 \text{ mA}/\text{cm}^2$ ). The XANES spectroscopy was conducted at BL12C, Photon Factory, Tsukuba, Japan (2011G151), and at BL14B2, SPring-8, Sayo, Japan (2012B1935), using a Mn  $K$ -edge to investigate the local electronic structures of the pristine and (de-)intercalated samples. The spectra were recorded in transmission mode. The XRD analysis was employed to examine the phases of the samples at a wavelength of

$0.5 \text{ \AA}$  and was conducted at BL19B2, SPring-8, Sayo, Japan (2012B1574).

## 3. Theoretical procedure

The first-principles calculations of the XANES spectra and the electronic structures were carried out using an all-electron full-potential linearized augmented plane wave plus local orbitals (FLAPW + lo) method as implemented in the WIEN2k density functional theory (DFT) code.<sup>18</sup> The spin-polarized generalized gradient approximation (GGA) and the self-interaction corrected (SIC)<sup>19</sup> GGA+ $U$  approaches within Perdew-Burke-Ernzerhof (PBE) exchange-correlation potential<sup>20</sup> were adopted in the present study. The effective intra-atomic correlation energies (Hubbard parameters)  $U_{\text{eff}}$  were taken to be 5.0 eV for the Mn  $d$  orbitals.<sup>21</sup> The plane wave cutoff  $R_{\text{MT}}K_{\text{max}}$  was fixed at 7.0 (Bohr  $\text{Ry}^{1/2}$ ), where  $R_{\text{MT}}$  is the smallest of all muffin-tin radii and  $K_{\text{max}}$  is the magnitude of the reciprocal-lattice vector. The  $R_{\text{MT}}$  automatically considered the lattice size and shape in the code. The energy threshold to separate the core and valence states was  $-9.0 \text{ Ry}$ .

The experimental crystallographic data of  $\text{Li}_x\text{Mn}_2\text{O}_4$  was used in the present theoretical calculations.<sup>22-25</sup> The crystallographic parameters and XANES calculation conditions are summarized in ESI, Table S1.†

The full structural optimizations for the two types of  $\text{Li}(\text{Mn}^{\text{III}}\text{Mn}^{\text{IV}})\text{O}_4$  were conducted using the Broyden-Fletcher-Goldfarb-Shanno (BFGS) algorithm<sup>26-28</sup> in the code. The full (single electron) core-hole effect was taken into account in the present XANES simulations, which virtually removed one electron from the  $1s$  orbital of an absorbing atom and added one electron to the bottom of the conduction band whose operation approximately corresponded to the final state of the X-ray absorption process. The use of a supercell with the core-hole effect is one of the standard methods, which can provide reasonable spectra compared with the experimental XANES spectra.<sup>29,30</sup> We also used this technique in our previous paper on the Co  $K$ -edge XANES in  $\text{Li}_x\text{CoO}_2$ .<sup>8</sup> The distance between two neighboring X-ray absorbing atoms, namely two adjacent core-holes, was longer than *ca.*  $8 \text{ \AA}$  for all supercells in Table S1, which was large enough to avoid interactions. The Brillouin zone integrations were performed using a tetragonal  $k$ -point mesh of the Monkhorst-Pack scheme.<sup>31</sup> The  $k$ -point grids used for the ground and excited states are also listed in ESI, Table S1.† The tolerances of the iterative self-consistent-field (SCF) procedure were fixed to 0.1 mRyd for the total energy and to  $10^{-3} e$  for the charge. The partial electronic density of states (PDOS) for the ground state and the XANES spectra for the excited states with a  $1s$  core-hole were calculated for all atoms in the cell and averaged with a weight factor. Both the XANES spectra for the allowed electronic dipole transitions and the PDOS were broadened by Gaussian functions with a full-width at half-maximum (FWHM) of 0.8 eV and 0.1 eV, respectively.

We do not intend to produce an exact reproduction of the experimental spectra using adjustable parameters, such as  $U_{\text{eff}}$ , non-integral electron core-hole effect, and so on.<sup>32,33</sup> We aim to interpret the features of the characteristic edge peaks and the discussed local structures in  $\text{Li}_x\text{Mn}_2\text{O}_4$ .

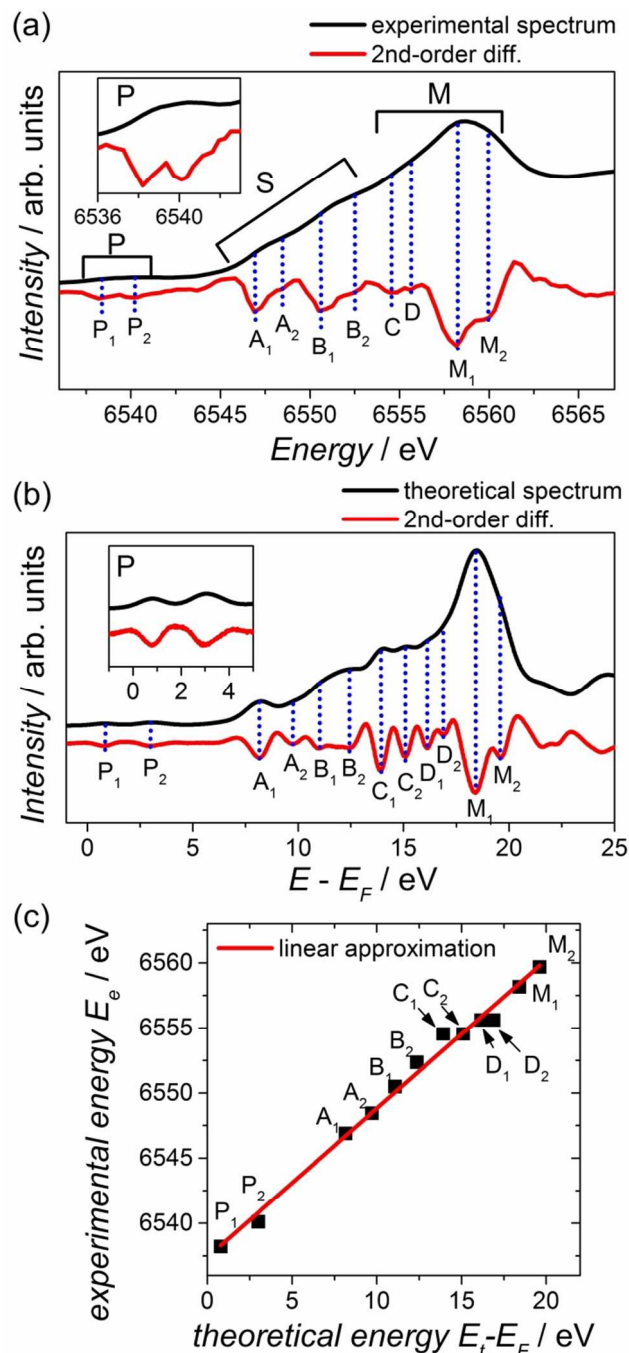


**Fig. 1** (a) Experimental Mn *K*-edge XANES spectrum and (b) theoretical spectrum calculated by GGA+*U* of LiMn<sub>2</sub>O<sub>4</sub>, respectively (black curves). Second-order differential curves of XANES spectra are also shown to clearly visualize each peak (red curves). (c) The comparative plots of theoretical peak energies with experimental ones ( $E_t - E_F = \alpha E_e + \beta$ ,  $\alpha = 1.14$ ,  $\beta = 6537.38$ ,  $R^2 = 0.991$ ).

## 4. Results and Discussion

### 4.1. Fingerprint Verification of Experimental/Theoretical Mn *K*-edge XANES Spectra of LiMn<sub>2</sub>O<sub>4</sub>.

The experimental Mn *K*-edge XANES spectrum of the LiMn<sub>2</sub>O<sub>4</sub> pristine sample is shown in Fig. 1(a). Most of the crests of the Mn *K*-edge XANES spectrum were caused by symmetry-allowed

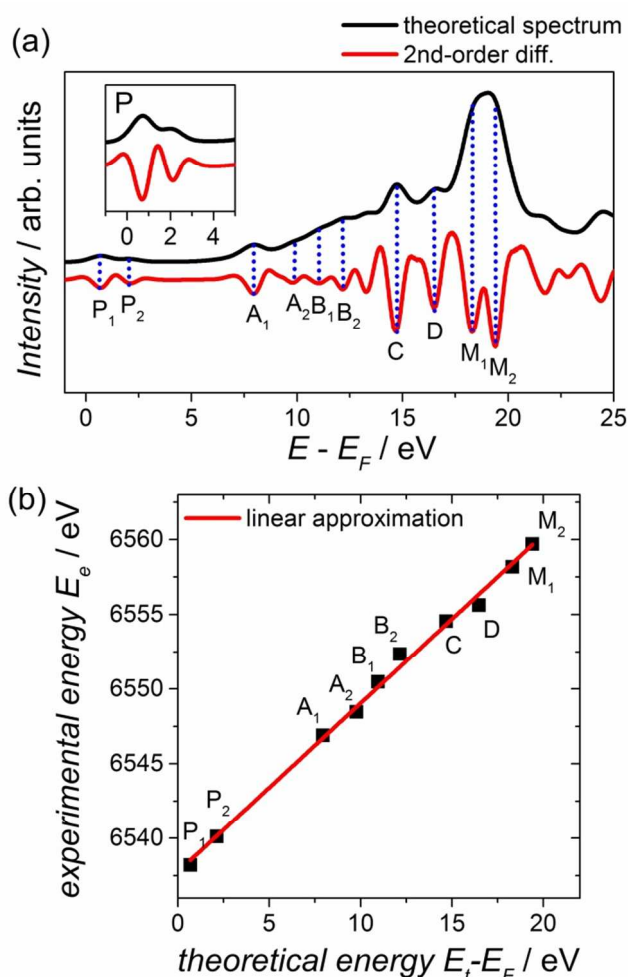


**Fig. 2** (a) Theoretical Mn *K*-edge XANES spectrum of LiMn<sub>2</sub>O<sub>4</sub> calculated by GGA (black curves). Second-order differential curves of the XANES spectra are also shown to clearly visualize each peak (red curves). (b) The comparative plots of the theoretical peak energies with experimental peak energies ( $E_t - E_F = \alpha E_e + \beta$ ,  $\alpha = 1.13$ ,  $\beta = 6537.79$ ,  $R^2 = 0.996$ ).

transitions from the 1*s* electron of manganese to the empty bands above Fermi energy *E<sub>F</sub>*. The transition-metal *K*-edge XANES spectrum can be discussed by three parts of the crests (regions M, S, and P in Figure 1(a)).<sup>34,35</sup> The main crests (region M) are assigned to the purely dipole-allowed 1*s* → 4*p* transition leading to the final state (1*s*<sup>1</sup>*c* 3*d*<sup>3.5</sup> 4*p*<sup>1</sup>), where *c* is a 1*s* core-hole. The shoulder crests (region S) are ascribed as the cause of the dipole-allowed 1*s* → 4*p* transition leading to the final state (1*s*<sup>1</sup>*c* 3*d*<sup>4.5</sup>*L* 4*p*<sup>1</sup>), with a shakedown process that originated from a ligand to metal charge transfer, where *L* is a ligand hole. The greatly weakened pre-edge absorption crests (region P) generally represent the electric dipole-forbidden transition of a 1*s* electron to an unoccupied 3*d* orbital (*t*<sub>2*g*</sub><sup>3</sup>*e*<sub>g</sub><sup>1</sup> in the Mn<sup>3+</sup> ion and *t*<sub>2*g*</sub><sup>3</sup>*e*<sub>g</sub><sup>0</sup> in the Mn<sup>4+</sup> ion). The theoretical XANES spectrum obtained by first-principles calculations is shown in Fig. 1(b). The effect of the core-hole was treated in the calculation for representing the shape of the spectrum. The second-order differential curves of the experimental and theoretical spectra (red curves) are also shown in order to clearly observe the peaks and easily permit a comparison. The experimental XANES spectrum was

well reproduced by the theoretical spectrum. In particular, the negative peaks of the second-order differential curve of the theoretical spectrum corresponding to the visible/invisible peaks in the spectrum resembled those of the experimental spectrum. The correlation between the peak energies of the experimental and theoretical spectra is summarized in Fig. 1(c). The linear approximation of the peak energies ( $E_t - E_F = \alpha E_e + \beta$ ,  $\alpha = 1.14$ ,  $\beta = 6537.38$ ) is shown by a red line, where  $E_t - E_F$  is the theoretical peak energy distance from  $E_F$ , and  $E_e$  is the experimental peak energy. The relatively high reliability of the approximation ( $R^2 = 0.991$ ) guarantees that the theoretical DFT calculation reproduces not only the characteristic parts of the crests (regions M, S, and P) but also the tiny peaks identified by the second-order differential processing.

In these calculations, we conventionally used GGA with the Hubbard parameter  $U_{eff}$  (GGA+ $U$ ). This parameter represents an effective on-site Coulomb correlation and has been commonly used to improve the description of the  $d$ -electron correlations for transition metal oxides.<sup>21</sup> In fact, the specific atomic and electronic structures around  $E_F$  in lithium manganese spinel oxide have been successfully reproduced by the GGA+ $U$  calculation. These atomic and electronic structures are the Jahn-Teller distortion and the localization of the  $d_z$  orbital, respectively.<sup>36-38</sup> Therefore, we are interested in understanding how the Hubbard parameter  $U_{eff}$  affects the representation of the XANES spectrum. The theoretical XANES spectrum calculated by GGA without  $U$  is shown in Fig. 2(a). The C and D peaks calculated by GGA are divided into two peaks, C<sub>1</sub>-C<sub>2</sub> and D<sub>1</sub>-D<sub>2</sub>, by GGA+ $U$  due to the expanded splitting gap between the up and down spin densities, which are shown in ESI, Fig. S2.† However, this difference was not important because the C and D peaks were broad and not clearly visible on the experimental spectrum. While the shape of the pre-edge peaks seems to be better represented by GGA+ $U$  than by GGA, the total spectrum shape could be simulated in either case (Fig. 1(b) and 2(a)). That is, the Hubbard parameter  $U_{eff}$  had less effect on the representation of the spectrum. Previously, we have reported on the experimental/theoretical Co K-edge XANES spectra of two types of lithium cobalt oxides, that is O3- and O2-LiCoO<sub>2</sub>.<sup>32</sup> A similar reproducibility has been reported in these compounds. However, the second-order difference processing has not been adapted yet. We would like to note that the tiny peaks on the experimental XANES spectra identified by this processing are also reproduced by the theoretical peaks in O3- and O2-LiCoO<sub>2</sub> as well as in LiMn<sub>2</sub>O<sub>4</sub> as shown in ESI, Fig. S3 and S4.†

#### 4.2. Verification of the Theoretical Mn K-edge XANES Spectra of LiMn<sub>2</sub>O<sub>4</sub> from the PDOS.

The PDOS of each element was estimated to discuss the contribution of the surrounding ions on the XANES spectrum. As shown in Fig. 3, the theoretical Mn K-edge XANES spectrum (black line) was represented by the Mn 4p PDOS (light purple area). The Mn 4p PDOS was overlapped with the O 2p PDOS (red area), especially around 5–16 eV (A–C peaks). The PDOS also overlapped with the Li 2p PDOS (yellow area). The charge transfer of an excited electron is caused by the transfer from the O 2p ligand orbital to Mn 4p and Li 2p metal orbitals at the overlap region. That is, the shakedown process, which is generally proposed for determining the shoulder peaks of the XANES spectrum, was well reproduced by the

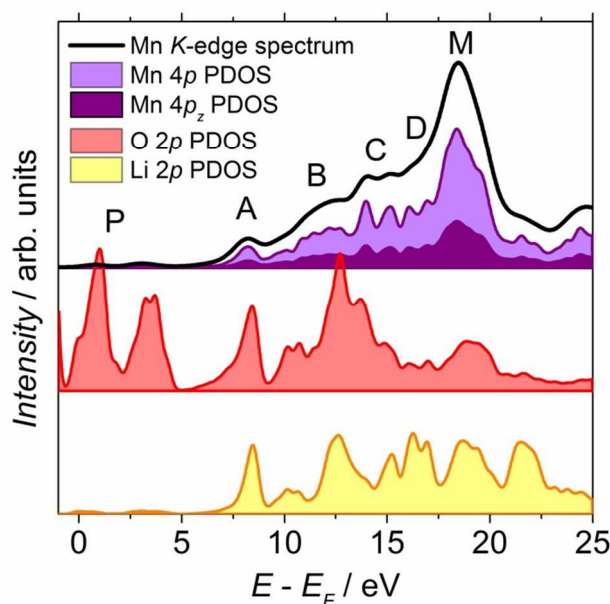


**Fig. 3** Partial density of states (PDOS) of the Mn total 4p-orbital (light purple area for total orbital and dark purple area for  $p_z$  orbital) of LiMn<sub>2</sub>O<sub>4</sub>. The partial density states of the O 2p-orbital (red area) and the Li 2p-orbital (yellow area) are also shown as well as the theoretical Mn K-edge XANES spectrum calculated by GGA+ $U$  (black curves).

DFT calculations. A similar correlation between the calculated PDOS and the XANES spectrum has been found at Co K-edge in LiCoO<sub>2</sub>.<sup>32</sup> In O3- and O2-layered LiCoO<sub>2</sub>, the anisotropic contributions between the Co 4p<sub>x</sub> + 4p<sub>y</sub> and 4p<sub>z</sub> PDOS to the XANES spectra was important for determining the shape of their XANES spectra and was related to the local structural difference around the absorbed cobalt center with their specific layer stacking. On the other hand, the anisotropic contribution differences between the Mn 4p<sub>x</sub>, 4p<sub>y</sub>, and 4p<sub>z</sub> PDOSs to the XANES spectrum were not identified in LiMn<sub>2</sub>O<sub>4</sub> because its spinel structure possesses a symmetric cubic structure. In fact, the Mn 4p<sub>z</sub> PDOS (dark purple area) was one third of the 4p total PDOS. Strictly, LiMn<sub>2</sub>O<sub>4</sub> has two electron-configuration characters, half of which are the Mn<sup>3+</sup> ion and half of which are the Mn<sup>4+</sup> ion, that were difficult to be distinguished by experimental tools because the electrons rapidly and continuously hop between the  $e_g$  orbitals on adjacent Mn<sup>3+</sup>/Mn<sup>4+</sup> ions.<sup>16</sup> Moreover, the LiMn<sub>2</sub>O<sub>4</sub> spinel structure is locally distorted by the Jahn-Teller effect of the Mn<sup>3+</sup>O<sub>6</sub> octahedral coordination although it has cubic symmetry. Thus, we attempted to separate the contribution of the Mn<sup>3+</sup> and Mn<sup>4+</sup> ions to the theoretical XANES spectrum using the DFT calculations. Anti-ferromagnetic (AFM) ordering models of LiMn<sub>2</sub>O<sub>4</sub> have been proposed for DFT calculations by various researchers,<sup>36,37</sup> which endorse the Goodenough-Kanamori rules.<sup>15,39</sup> Ouyang *et al.* have shown two possible AFM configurations, as shown in Fig. 4.<sup>36</sup> The first configuration is an AFM-1 model with the ordering of manganese chains along the [110] direction of the  $Fd-3m$  symmetry, and the space group of the reorganized primitive cell is the monoclinic  $C2/c$ . The other configuration is an AFM-2 model arranged as a planer AFM with alternating spin-up and spin-down manganese atoms within the (110) planes of the  $Fd-3m$  symmetry, and the space group of the reorganized primitive cell is



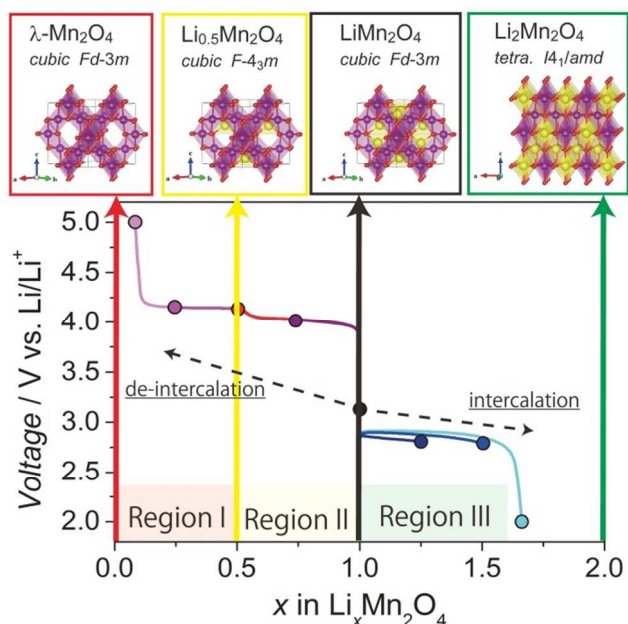


**Fig. 6** Schematic diagram of the phase transitions during de-intercalation or intercalation from  $\text{Li}_x\text{Mn}_2\text{O}_4$  ( $x = 1$ ). Purple octahedrons represent  $\text{MnO}_6$ , red balls indicate oxide ions, and yellow balls represent lithium ions. The bottom figure shows the electrochemical lithium-ion (de-)intercalation profiles in this study determined by the galvanostatic method (C rate: 0.1 C). The circles indicate samples analyzed by XAFS measurements.

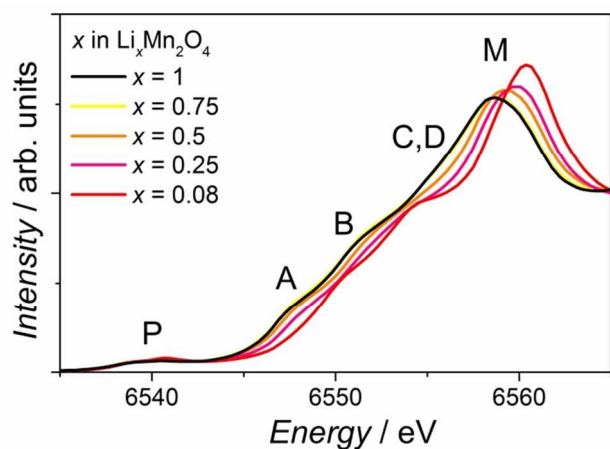


**Fig. 7** Experimental Mn K-edge XANES spectra of samples of de-intercalated lithium ions from  $\text{Li}_x\text{Mn}_2\text{O}_4$  ( $x = 1$ ).

lithium ion is removed/inserted.) The pristine  $\text{LiMn}_2\text{O}_4$  powder in this study was cooled during synthesis at a slow rate to prevent the oxygen non-stoichiometry as much as possible. Consequently, three distinct regions (I to III) were visible in Fig. 6 without requiring the additional regions around 3.3 and 4.5 V reported in Ref. 17. The circles in Fig. 6 indicate the various lithium-ion de-intercalated or intercalated states in the  $\text{Li}_x\text{Mn}_2\text{O}_4$  samples for XANES measurements. The value of  $x$  in  $\text{Li}_x\text{Mn}_2\text{O}_4$  was calculated by assuming that all electric currents were utilized for the lithium-ion de-intercalation or intercalation processes. The crystal structure of the experimental sample of each  $x$  value has been reported before, and the cell models used in these calculations reflected the published

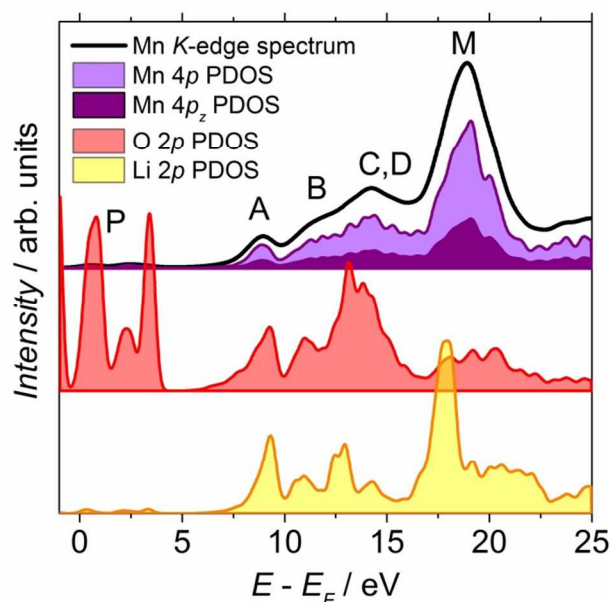


**Fig. 8** Partial density of states (PDOS) of the Mn  $4p$  orbital (light purple area for the total orbital and dark purple area for the  $p_z$  orbital) of  $\text{Li}_{0.5}\text{Mn}_2\text{O}_4$ . The partial density states of the O  $2p$  orbital (red area) and the Li  $2p$  orbital (yellow area) are also shown as well as the theoretical Mn K-edge XANES spectrum calculated by GGA+ $U$  (black curves).

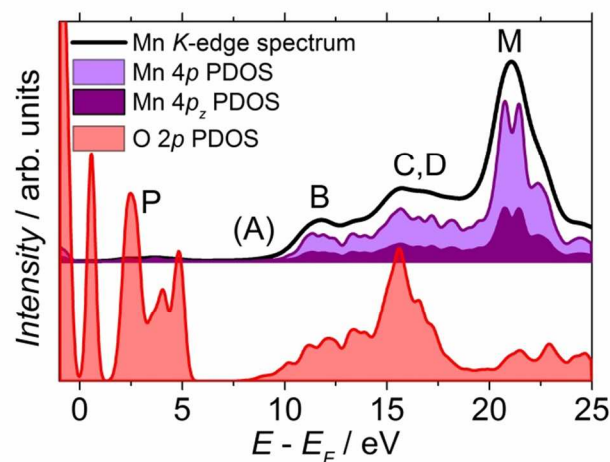


**Fig. 9** Partial density of states (PDOS) of Mn  $4p$  orbital (light purple area for total orbital and dark purple area for  $p_z$  orbital) of  $\lambda\text{-MnO}_2$ . The partial density states of the O  $2p$  orbital (red area) is also shown as well as the theoretical Mn K-edge XANES spectrum calculated by GGA+ $U$  (black curves).

experimental crystallographic information. The resulting  $x$  values are  $\text{Li}_{0.5}\text{Mn}_2\text{O}_4$  at the middle point between Regions I and II,  $\lambda\text{-MnO}_2$  at the end point of Region I, and  $\text{Li}_2\text{Mn}_2\text{O}_4$  at the end point of Region III.<sup>22-25</sup> We also measured the synchrotron X-ray diffraction patterns for estimating the ratios of the phases at each  $x$  value in this experimental study, which are summarized in ESI, Table S2.†

The experimental Mn K-edge XANES spectra of the samples ( $x = 0.75, 0.5, 0.25, 0.08$ ) de-intercalated from  $\text{LiMn}_2\text{O}_4$  as well as the pristine sample are shown in Fig. 7. The main peak M, shoulder peaks A–D, and pre-edge peak P described in pristine  $\text{LiMn}_2\text{O}_4$  were also observed in the de-intercalated samples; however, each peak

was changed slightly by these compositions, and these changes could be separated into Regions I and II. For  $x \geq 0.5$  (Region II), no significant change could be observed around the A–C peaks, although the M peak slightly shifts to a higher energy. Additionally, for  $x < 0.5$  (Region I), the B and C–D peaks shift to lower energies, and the intensities of these peaks decreased in addition to the obvious shift of the M peak to a higher energy. Moreover, the intensity of the A peak significantly decreases.

Owing to these differences in response to the structural changes, the theoretical XANES spectra of  $\text{Li}_{0.5}\text{Mn}_2\text{O}_4$  and  $\lambda\text{-MnO}_2$  were calculated, which are shown by black lines in Fig. 8 and 9, respectively. The theoretical XANES spectra successfully reproduced the experimental spectra shown in Fig. 7. The theoretical spectrum of  $\text{Li}_{0.5}\text{Mn}_2\text{O}_4$  was roughly similar to that of pristine  $\text{LiMn}_2\text{O}_4$ , although the M peak slightly shifted from 18.4 to 18.9 eV vs.  $E_F$ . (The top of the experimental peak also shifted from 6558.6 ( $x = 1$ ) to 6559.2 ( $x = 0.5$ ) eV.) At the end of Region II ( $x = 0.5$ ), the Mn 4p PDOS (light purple area) related to the localized M peak more than that at  $x = 1$  due to the oxidation of the Mn valence state from 3.5+ to 3.75+. However, the approximate structural environment around the Mn atom was maintained, and the shapes of the Mn 4p and O 2p PDOS looked similar. Thus, no significant change can be observed around shoulder A–D peaks. In addition, the theoretical spectrum of  $\lambda\text{-MnO}_2$  was clearly different from those of pristine  $\text{LiMn}_2\text{O}_4$  and  $\text{Li}_{0.5}\text{Mn}_2\text{O}_4$ . The M peak shifts to 20.1 eV vs.  $E_F$ . (The top of the experimental peak shifts to 6560.4 at  $x = 0.08$ .) This is also due to the localization of the Mn 4p PDOS with the oxidation of the Mn valence state. Additionally, the A peak disappears on the  $\lambda\text{-MnO}_2$  spectrum. Around the A peak, the Mn 4p PDOS of pristine  $\text{LiMn}_2\text{O}_4$  and  $\text{Li}_{0.5}\text{Mn}_2\text{O}_4$  overlapped with the O 2p PDOS (red area). Furthermore, the Mn 4p PDOS also indirectly overlapped with the Li 2p PDOS (yellow area) via the O 2p PDOS. However, the Li 2p PDOS could not contribute to the shape of the Mn 4p PDOS, which is the Mn K-edge XANES spectrum, in the non-lithium containing  $\lambda\text{-MnO}_2$ . Thus, the shape of the XANES spectrum was significantly changed by the indirect contribution of the Li 2p PDOS via the O 2p PDOS even though the approximate structural environment around the Mn atom was similar. Moreover, these results could be determined by comparing the PDOS of each element to the well-reproduced theoretical XANES simulations. As an aside, the anisotropic contribution differences among  $4p_x$ ,  $4p_y$ , and  $4p_z$  PDOS to the XANES spectrum were not identified because of the symmetric cubic  $\text{Li}_{0.5}\text{Mn}_2\text{O}_4$  and  $\lambda\text{-MnO}_2$  structures. The Mn  $4p_z$  PDOS (dark purple) was one third of the 4p total PDOS in these compounds.

#### 4.4. Change in the Mn K-edge XANES Spectra of $\text{Li}_x\text{Mn}_2\text{O}_4$ ( $x > 1$ ) during the lithium-ion intercalation process.

The experimental Mn K-edge XANES spectra of the samples ( $x = 1.25, 1.5, 1.66$ ) intercalated from  $\text{LiMn}_2\text{O}_4$  as well as pristine sample are shown in Fig. 10. The M (overlapped with C and D), A, B, and P peaks were also observed in the intercalated samples, while an impressive change of the XANES spectra was observed as compared to the de-intercalated samples. The M peak broadened and shifted to lower energy. Moreover, we observed a noticeable increase of the crest around peak A. These interesting changes are

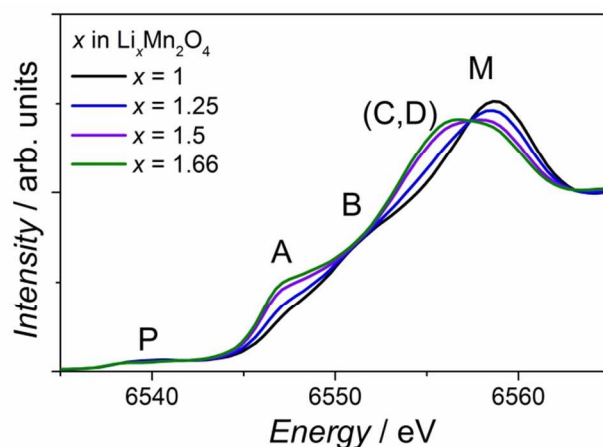


Fig. 10 Experimental Mn K-edge XANES spectra of samples of intercalated lithium ions from  $\text{Li}_x\text{Mn}_2\text{O}_4$  ( $x = 1$ ).

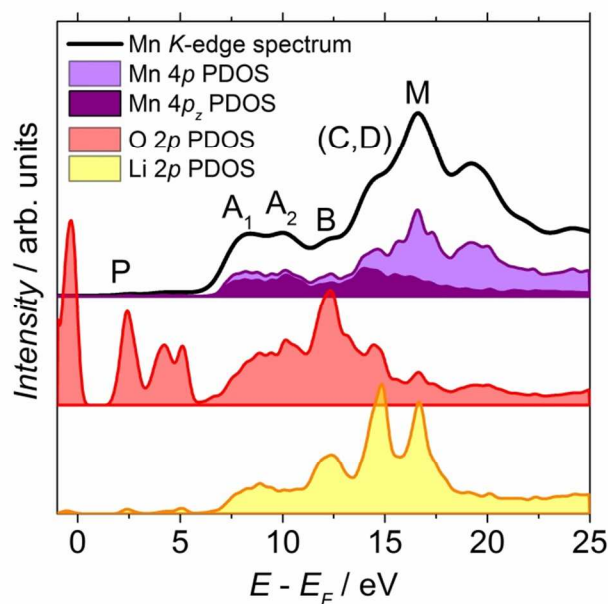


Fig. 11 Partial density of states (PDOS) of the Mn 4p orbital (light purple area for total orbital and dark purple area for  $p_z$  orbital) of  $\text{Li}_2\text{Mn}_2\text{O}_4$ . The partial density states of the O 2p orbital (red area) and the Li 2p orbital (yellow area) are also shown as well as the theoretical Mn K-edge XANES spectrum calculated by GGA+U (black curves).

due to the phase transition from the cubic phase to the tetragonal phase. Therefore, the theoretical XANES spectrum of the  $\text{Li}_2\text{Mn}_2\text{O}_4$  tetragonal phase was calculated to investigate the differences in the response to structural changes, which is shown by a black line in Fig. 11. The theoretical spectrum of  $\text{Li}_2\text{Mn}_2\text{O}_4$  was clearly different from those of pristine  $\text{LiMn}_2\text{O}_4$  and seemed to be similar to the experimental spectrum of  $\text{Li}_{1.66}\text{Mn}_2\text{O}_4$ , which contains 77.4% of the  $I4_1/amd$  tetragonal phase. The M peak shifted from 18.4 to 16.6 eV vs.  $E_F$  due to the reduction of the Mn valence state from 3.5+ to 3+. (The top of the experimental peak also shifted from 6558.6 ( $x = 1$ ) to 6556.8 ( $x = 1.66$ ) eV.) The Mn 4p PDOS (light purple area) near the M peak broadened and split because this state was delocalized by the partial contribution of O 2p PDOS. Moreover, the anisotropic contribution differences between  $4p_x + 4p_y$  and  $4p_z$  PDOS to the

XANES spectrum could be identified. The other significant change could be seen at the A peak, which also split into two peaks ( $A_1$  and  $A_2$ ), which is due to the phase transition from the cubic  $Fd-3m$  phase to the tetrahedral  $I4_1/amd$  phase. Between the two phases, there is a difference in the coordination of lithium ion, which occupied the tetrahedral site at the  $Fd-3m$  phase and the octahedral site at  $I4_1/amd$  phase. That is, the indirect contribution of the Li  $2p$  PDOS to the Mn  $4p$  PDOS via the O  $2p$  PDOS at the A peak was different between the two phases. Overall, the shift of the M peak with the Mn valence state change during the intercalation process ( $1 < x < 2$ ) in  $\text{Li}_x\text{Mn}_2\text{O}_4$  can be explained by the localizing degree of the Mn  $4p$  PDOS in common with de-intercalation process ( $0 < x < 1$ ). On the other hand, the contribution between the Mn  $4p$  PDOS and the surrounding atom PDOS is important for understanding the features of the A–B peaks, which are generally called shoulder peaks. In particular, the coordination of lithium to oxygen would dominate the shape of the A peak. Additional proof can be seen at the theoretical Mn  $K$ -edge spectrum of  $\text{Li}_2\text{MnO}_3$ , in which the lithium ion was octahedrally coordinated to the O atoms, as calculated by other groups.<sup>33</sup> The splitting of the A peak ( $A_1$  and  $A_2$ ) in the  $\text{Li}_2\text{Mn}_2\text{O}_4$   $I4_1/amd$  phase has been also seen in the  $\text{Li}_2\text{MnO}_3$   $C2/m$  phase, although the Mn valence states were different from each other ( $3+$  at  $\text{Li}_2\text{Mn}_2\text{O}_4$  and  $4+$  at  $\text{Li}_2\text{MnO}_3$ , respectively.) Thus, these results suggest that the coordination of the lithium ion could be detected by the shoulder peak of the Mn  $K$ -edge XANES spectrum in lithium-manganese-based phases. Moreover, similar lithium ion contributions to the spectrum have been seen at the experimental and theoretical Co  $K$ -edge XANES spectra of  $\text{LiCoO}_2$ , which is the Co  $4p$  PDOS overlapped with the nearby Li  $2p$  PDOS via the O  $2p$  PDOS.<sup>8</sup>

## Conclusions

We compared the experimental and theoretical Mn  $K$ -edge XANES spectra of  $\text{LiMn}_2\text{O}_4$ . Both the easily observed parts and the tiny peaks of the theoretical Mn  $K$ -edge XANES spectra agreed with the experimental spectra. That is, first-principles calculations are a powerful technique for determining the shape of the Mn  $K$ -edge spectrum. We also calculated the theoretical XANES spectra of two anti-ferromagnetic  $\text{LiMn}_2\text{O}_4$  models for demonstrating Jahn-Teller character of  $\text{Mn}^{3+}$  ion. The results suggest that the  $4p_z$  orbital of  $\text{Mn}^{3+}$  ion could be stabilized by the lengthening of the Mn–O bond along the  $z$  axis. Therefore, the Jahn-Teller distortion affects not only the  $3d$ -levels but also the  $4p$  orbital spreading through the empty band.

Our calculations also explained the experimental spectral changes during the de-intercalation process of  $\text{Li}_x\text{Mn}_2\text{O}_4$  ( $x = 0 - 1$ ). Specifically, the shift of the M peak to a higher energy and the disappearance of the A peak at these regions are understood from the interaction between the Mn  $4p$  orbital and the Li  $2p$  orbital via the O  $2p$  orbital. On the other hand, during the intercalation process of  $\text{Li}_x\text{Mn}_2\text{O}_4$  ( $x = 1 - 2$ ), the shapes of the XANES contributions of the  $\text{Mn}^{3+}$  ion and  $\text{Mn}^{4+}$  ion centers to the spectra differ due to the difference in the corresponding PDOS overlap with the O  $2p$  PDOS. The XANES spectral changes with the lithium ion displacement (six- to four-coordination) along with the phase transition (cubic  $Fd-3m$  to tetragonal  $I4_1/amd$ ) are determined by the indirect contribution of the Li  $2p$  PDOS to the Mn  $4p$  PDOS via the O  $2p$  PDOS.

Overall, the differences in the shape of the XANES spectra of lithium manganese oxides as result of the lithium content, the Jahn-Teller effect, and/or the phase transition were analyzed by DFT calculations of the Mn  $K$ -edge XANES spectra. The experimental transition-metal XANES spectra were useful for determining the valence change of the redox ions in the materials of lithium ion batteries. However, the crystal structural changes during lithium battery reactions are difficult to understand using only the experimental spectra. The findings in this study are useful for understanding the degradation of lithium manganese-based phases and the complex electrochemical reaction that occurs in  $\text{Li}_2\text{MnO}_3$ - $\text{LiMO}_2$  solid solutions by the richly-resolved XANES technique, which can be further combined with *in-situ*, small area, and/or short time scale measurements.

## Acknowledgements

This work was supported by the New Energy Promotion Council (NEPC) and the Japan Automobile Research Institute (JARI). All of the crystal structures were drawn with the help of VESTA software.<sup>40</sup>

## Notes and references

National Institute of Advanced Industrial Science and Technology (AIST), Midorigaoka 1-8-31, Ikeda, Osaka 563-8577, Japan. \*E-mail: toyoki-okumura@aist.go.jp; hironori-kobayashi@aist.go.jp

† Electronic supplementary information (ESI) available. See DOI: 10.1039/b000000x/

- M. Tada, S. Murata, T. Asakoka, K. Hiroshima, K. Okumura, H. Tanida, T. Uruga, H. Nakanishi, S. Matsumoto, Y. Inada, M. Nomura, Y. Iwasawa, *Angew. Chem. Int. Ed.*, 2007, **46**, 4310.
- N. Ishiguro, T. Saida, T. Uruga, S. Nagamatsu, O. Sekikawa, K. Nitta, T. Yamamoto, S. Ohkoshi, Y. Iwasawa, T. Yokoyama, M. Tada, *ACS Catal.*, 2012, **2**, 1319.
- N. Ishiguro, T. Saida, T. Uruga, O. Sekikawa, K. Nagasawa, K. Nitta, T. Yamamoto, M. Tada, *Phys. Chem. Chem. Phys.*, 2013, **15**, 18827.
- T. Nonaka, C. Okuda, Y. Seno, H. Nakano, K. Koumoto, Y. Ukyo, *J. Power Soc.*, 2006, **162**, 1329.
- M. Menzel, A. Schlifke, M. Falk, J. Janek, M. Fröba, U. Elisabeth, A. Fittschen, *Spectrochim. Acta B*, 2013, **85**, 62.
- T. Okumura, T. Fukutsuka, K. Matsumoto, Y. Orikasa, H. Arai, Z. Ogumi, Y. Uchimoto, *Dalton Trans.*, 2011, **40**, 9752.
- I. Tanaka, T. Mizoguchi, T. Yamamoto, *J. Am. Ceram. Soc.*, 2005, **88**, 2013.
- T. Okumura, Y. Yamaguchi, M. Shikano, H. Kobayashi, *J. Mater. Chem.*, 2012, **22**, 17340.
- F. T. Wagner, B. Lakshmanan, M. F. Mathias, *J. Phys. Chem. Lett.*, 2010, **1**, 2204.
- T. Numata, C. Amemiya, T. Kumeuchi, M. Shirakata, M. Yonezawa, *J. Power Sources*, 2001, **97-98**, 358.
- S. T. Myung, M. H. Cho, H. T. Hong, T. H. Kang, C. S. Kim, *J. Power Sources*, 2005, **146**, 222.
- J. Belt, V. Utgikar, I. Bloom, *J. Power Sources*, 2011, **196**, 10213.
- R. Santanam, B. Rambabu, *J. Power Sources*, 2010, **195**, 5442.

- 14 A. Sakunthala, M.V. Reddy, S. Selvasekarapandian, B.V.R. Chowdaria, P. Christopher Selvin, *Electrochimica Acta.*, 2010, **55**, 4441.
- 15 J. B. Goodenough, A. Manthiram, B. Wnetrzewski, *J. Power Sources*, 1993, **43-44**, 269.
- 16 Y. J. Lee, F. Wang, C. P. Grey, *J. Am. Chem. Soc.*, 1998, **120**, 12601.
- 17 T. Ohzuku, M. Kitagawa, T. Hirai, *J. Electrochem. Soc.*, 1990, **137**, 769.
- 18 P. Blaha, K. Schwarz, G. K. H. Madsen, D. Kvasnicka, J. Luitz, *Computer code WienK, An Augmented Plane Wave + Local Orbitals Program for calculating Crystal Properties*, K. Schwarz, Techn. Universitat Wien, Austria, 2001.
- 19 V. I. Anisimov, I. V. Solovyev, M. A. Korotin, M. T. Czyżyk, G. A. Sawatzky, *Phys. Rev. B*, 1993, **48**, 16929.
- 20 J. P. Perdew, K. Burke, M. Ernzerhof, *Phys. Rev. Lett.*, 1996, **77**, 3865.
- 21 F. Zhou, M. Cococcioni, C. M. Marianetti, D. Morgan, G. Ceder, *Phys. Rev. B*, 2004, **70**, 235121.
- 22 J. Akimoto, Y. Takahashi, Y. Gotoh, S. Mizuta, *Chem. Mater.*, 2000, **12**, 3246.
- 23 J. Akimoto, Y. Takahashi, Y. Gotoh, S. Mizuta, *J. Cryst. Growth*, 2001, **229**, 405.
- 24 K. Ariyoshi, Y. Iwakoshi, N. Nakayama, T. Ohzuku, *J. Electrochem. Soc.*, 2004, **151**, A296.
- 25 A. S. Wills, N. P. Raju, C. Morin, J. E. Greedan, *Chem. Mater.*, 1999, **11**, 1936.
- 26 C. G. Broyden, *SIAM J. Appl. Math.*, 1970, **6**, 76.
- 27 R. Fletcher, *Comput. J.*, 1970, **J13**, 317.
- 28 D. Goldfarb, *Math. Comput. Modell.*, 1970, **24**, 23.
- 29 I. Tanaka, T. Mizoguchi, *J. Phys.: Condens. Matter*, 2009, **21**, 104201.
- 30 W.-Y. Ching, P. Rulis, *J. Phys.: Condens. Matter*, 2009, **21**, 104202.
- 31 H. J. Monkhorst, J. D. Pack, *Phys. Rev. B*, 1976, **13**, 5188.
- 32 A. Juhin, F. de Groot, *Phys. Rev. B*, 2010, **81**, 115115.
- 33 T. Tamura, T. Ohwaki, A. Ito, Y. Ohsawa, R. Kobayashi, S. Ogata, *Modelling Simul. Mater. Sci. Eng.*, 2012, **20**, 1.
- 34 B. Ammundsen, D. J. Jones, J. Rozière, *Chem. Mater.*, 1996, **8**, 2799.
- 35 C. R. Horne, U. Bergmann, M. M. Grush, R. C. C. Parera, D. L. Ederer, T. A. Callcott, E. J. Cairns, S. P. Cramer, *J. Phys. Chem. B*, 2000, **104**, 9587.
- 36 C. Y. Ouyang, S. Q. Shi, M. S. Lei, *J. Alloys Compd.*, 2009, **474**, 370.
- 37 G. Singh, S. L. Gupta, R. Prasad, S. Auluck, R. Gupta, A. Sil, *J. Phys. Chem. Solids*, 2009, **70**, 1200.
- 38 B. Xu, S. Meng, *J. Power Sources*, 2010, **195**, 4971.
- 39 J. Kanamori, *J. Phys. Chem. Solid*, 1959, **10**, 87.
- 40 R. West, *Basic Solid State Chemistry*, John Wiley and Sons Ltd., USA, 1984.
- 41 K. Momma, F. Izumi, *J. Appl. Crystallogr.*, 2011, **44**, 1272.